

# A Current Reconstruction Algorithm for Three-Phase Inverters Using Integrated Current Sensors in the Low-Side Switches

Sibaprasad Chakrabarti

Thomas M. Jahns

Robert D. Lorenz

Department of Electrical and Computer Engineering

University of Wisconsin-Madison

1415 Engineering Drive

Madison, WI, USA 53706

sib@cae.wisc.edu

jahns@engr.wisc.edu

lorenz@engr.wisc.edu

**Abstract**— Power semiconductor switches that include integrated pilot current sensors create opportunities to eliminate external current sensors in three-phase inverter applications. Each of the three conventional low-side power switches in a three-phase inverter can be replaced by one of these special devices that is designed to provide a sensing level current that accurately mirrors its total forward current. Recognizing that the output current in each phase flows through the low-side switch for only a portion of the fundamental cycle, a technique has been developed to reconstruct the full phase current waveforms for  $R$ - $L$  loads using only the incomplete phase current measurements. The performance characteristics of the proposed current reconstruction technique are experimentally verified, including demonstration of a closed-loop three-phase current regulator using the reconstructed current feedback from the integrated pilot current sensors.

**Keywords:** Current sensors, pilot current sensing, pulse width modulated inverters, power MOSFETs, insulated gate bipolar transistors

## I. INTRODUCTION

Three-phase voltage-source PWM inverters with closed-loop current regulators are widely used in many applications. Galvanically-isolated current sensors such as Hall-effect detectors placed in flux concentrating toroidal cores are typically introduced into at least two of the inverter output lines in order to provide the needed current feedback signals. Such field-based current sensors perform well but are typically quite expensive and too bulky to be easily integrated inside power modules. Recent work using miniature giant magnetoresistive field detectors as galvanically-isolated current sensors has shown that such methods perform well and are suitable for cost effective integration inside modules [1]. However, such field detector methods are dependent on the spatial distribution of magnetic fields inside of modules, which makes them challenging to integrate. Non-galvanically-isolated approaches such as current shunt resistors with level-shifting integrated circuits can be cost effective alternatives for some power module applications, but the associated power dissipation becomes more troublesome

as the load power rating increases and lack of isolation can lead to performance compromises.

Estimation approaches to reduce the number of current sensors are also candidates. One approach is to use a single current sensor to measure the dc link current and estimate (reconstruct) the phase currents using the active voltage vector timing [2-4]. Unfortunately, this method encounters limitations when the duration of the active states becomes very short (i.e., low output voltage conditions).

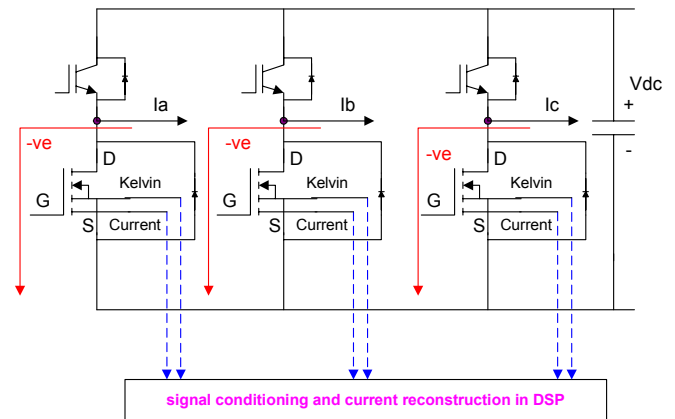


Fig. 1: Three-phase voltage-source inverter with integrated current sensors in the three low-side switches.

Increased pressure to reduce cost by integrating more functionality into power modules is creating renewed interest in integrated pilot current sensors [5,6] as a promising means to integrate accurate, current feedback information. Integrated pilot current sensors are already widely used in commercially-produced power modules for purposes of overcurrent protection, and work is under way to improve the linearity and dynamic performance characteristics of these devices for use in current regulation circuits.

This paper presents a new technique for reconstructing the phase currents in a three-phase inverter using current measurements from integrated pilot current sensors placed in

This work was supported primarily by the ERC Program of the National Science Foundation under Award Number EEC-9731677.

the three low-side inverter power switches (see Fig. 1). Although the figure shows integrated current sensors in power MOSFETs for the low-side inverter switches, past work has also demonstrated the feasibility of introducing such integrated sensors into IGBTs as well [6].

Since the output phase current passes through the low-side switch for only a portion of the fundamental cycle, special steps must be taken to cope with the incomplete current feedback information. This paper demonstrates how the available information can be utilized effectively to reconstruct the full output phase current waveforms in three-phase  $R$ - $L$

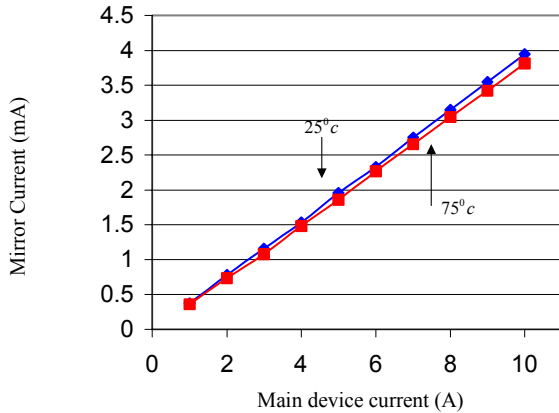


Fig. 2: Measured pilot current sensor characteristics for a 400V, 10A power MOSFET (IR Model IRFC740)

loads, making it possible to achieve high-performance closed-loop current regulation. Experimental results are presented to verify the proposed technique.

## II. PILOT CURRENT SENSOR CHARACTERISTICS

Commercially-available power MOSFETs equipped with integrated pilot current sensors have been tested to investigate the linearity of the current sense ratio and its sensitivity to change in temperature over the operating range specified by the manufacturer. The particular device selected for the tests described here is a 400V, 10A power MOSFET (Model IRFC740) manufactured by International Rectifier.

Figure 2 shows the measured current sensing characteristics of this power MOSFET for two different operating temperatures. The well-known virtual-ground inverting op-amp configuration [7] was used as the signal conditioning to perform the current-to-voltage conversion without loading the device. The test results exhibit very good linearity between the drain current and the sensed current over the entire operating current range. This figure also shows that the relationship is quite insensitive to changes in device temperature.

It is worth noting that the sensing capabilities of the integrated pilot current sensor are useful only when the current is flowing through the MOSFET in the forward direction. This characteristic limits the completeness of the current feedback information that can be provided by the device when it is used in an inverter phase-leg configuration such as Fig. 1.

Separate testing of the frequency response of the pilot current sensors has indicated that their bandwidth approaches 1 MHz, meeting the dynamic response requirements for many high-performance motor drive current regulators. Further investigation of the performance of these pilot current during switching operation indicates that the fidelity of the output current sense signal is corrupted by switching noise during the turn-on and turn-off transitions. However, this characteristic does not hinder the use of the pilot current sensors provided that care is taken to avoid sampling the currents during the transition intervals when the device is being gated on or off.

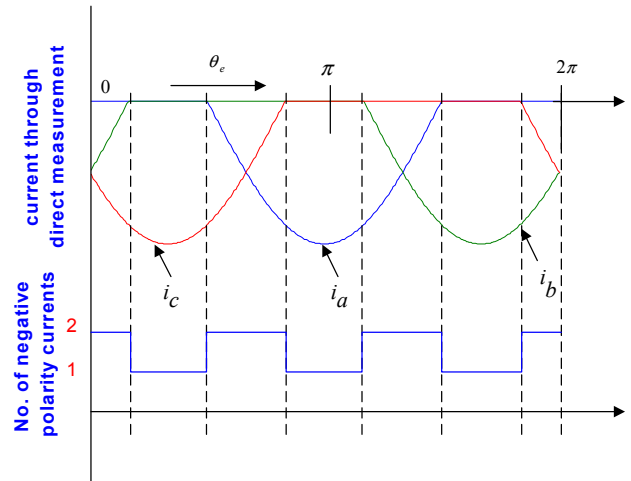


Fig. 3: Sensed currents during balanced three-phase excitation using integrated pilot current sensors sampled once per PWM switching cycle

These test results suggest that integrated pilot current sensors can be designed with sufficient linearity and frequency response to make them candidates for use in closed-loop current regulators with both passive and motor loads. Although power MOSFETs were used during this investigation, a separate project is under way to verify that IGBTs can also be designed with pilot current sensors delivering comparable performance.

## III. CURRENT SAMPLING TECHNIQUE

During PWM operation of the inverter in Fig. 1, the phase current flows through each low-side MOSFET in the forward direction only when the polarity of the associated phase current is negative. (By convention, the inverter phase current is considered to be positive when it is flowing out of the phase-leg output terminal.)

Only the low-side switches in this inverter include the integrated current sensors since pilot sensors in the high-side switches would require high-performance level shifting to transfer the sensor signals to a common reference voltage. In contrast, the three pilot sensors in the three lower switches of Fig. 1 already share the same reference terminal (i.e., the negative bus), simplifying the signal conditioning. However, in exchange for this advantage, the Fig. 1 configuration limits the measurable current measurements to the negative-polarity

portions of each of the three phase currents, as indicated in Fig. 3.

Given these constraints and balanced three-phase excitation, at least one and at most two of the three phase currents can be sensed at any time instant. More specifically, intervals when one or two phase currents can be measured alternate in 60 degree bands as shown in Fig. 3. It is important to note that there are no time instants when all three of the phase currents can be measured simultaneously using this type of inverter configuration.

Since simultaneous sampling of the phase currents is desirable, the accessible phase currents are sampled only when

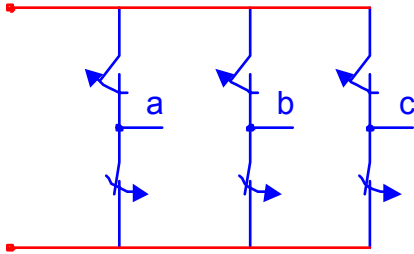


Fig. 4: Zero-voltage (000) inverter PWM state.

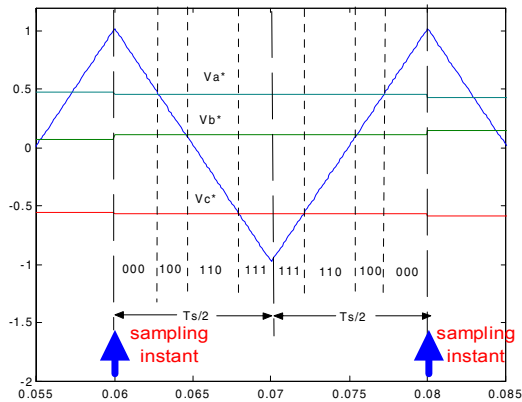


Fig. 5: Equivalent SVPWM timing diagram for current sampling during a PWM switching cycle

the zero-voltage space vector (000) is applied, assuming space vector pulse width modulation (SVPWM). This zero (000) vector corresponds to the inverter condition when all three of the lower switches are gated on, as shown in Fig. 4.

The current sampling instant is selected to occur at the approximate midpoint of each PWM timing interval when the zero (000) voltage vector is applied. This sampling approach is illustrated in Fig. 5 using an equivalent sine-triangle comparison method where an appropriate zero-sequence component is added to the sinusoidal three-phase current references. The PWM frequency is high compared to the fundamental frequency so that the three voltage reference waveforms look like nearly horizontal lines in this figure. As indicated in Fig. 5, current sampling is timed to occur at the peaks of the triangle carrier waveform.

This approach offers two advantages. First, the sampling instant will be displaced in time from the phase-leg transition instants when the current references and triangle wave intersect in Fig. 5, provided that the modulation index is less than one. This approach reduces the noise content in the sensed current signal caused by the power switch current transitions as described in the preceding section.

As a second advantage, it has been shown in previous work [8] that this synchronous sampling technique has the advantage of minimizing the impact of switching ripple components on the measured phase currents. Provided that the two complementary zero voltage vectors (000 and 111) are

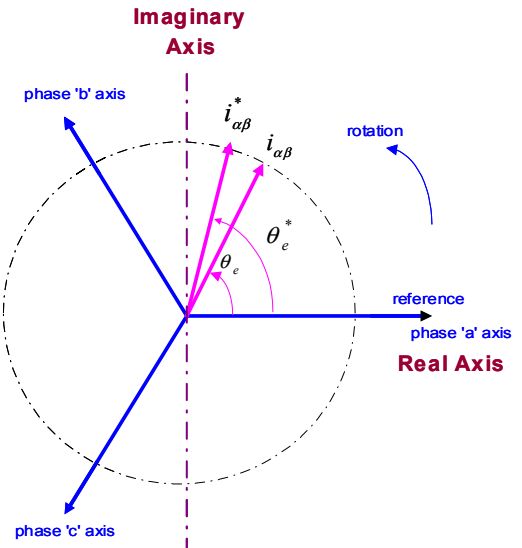


Fig. 6: Instantaneous complex current vectors showing current command vector  $i_{\alpha\beta}^*$  and the actual phase current vector  $i_{\alpha\beta}$

nearly equal in length, the sampled currents using this approach will closely correspond to the desired instantaneous values of the fundamental-frequency phase current components for the three phases.

#### IV. PHASE CURRENT RECONSTRUCTION ALGORITHM

Using conventional terminology, the two-phase complex current vector in the stationary reference frame is defined as

$$i_{\alpha\beta} = \frac{2}{3} [i_a + e^{-j2\pi/3} i_b + e^{j2\pi/3} i_c] \quad (1)$$

where  $i_a$ ,  $i_b$  and  $i_c$  are the instantaneous phase currents in the stationary frame. It is assumed that the machine is wye-connected with a floating neutral so that there is no zero-sequence component (i.e.,  $i_a + i_b + i_c = 0$  at all times).

Figure 6 provides a view of the complex current command vector  $i_{\alpha\beta}^*$  and the actual phase current vector  $i_{\alpha\beta}$  in the space

vector plane at one time instant. The difference between these two vectors represents the current error.

This complex vector representation makes it convenient to visualize the conditions under which each phase current is measurable using the inverter configuration in Fig. 1. Selecting phase *a* as an example, Fig. 7 shows that there are two polar arc sectors in which the phase *a* current  $i_a$  is measurable, and two intervening arc sectors where it is not measurable. More specifically,  $i_a$  flows through the low-side switch and can be sensed directly using the sampling technique described earlier whenever the phase current vector  $i_{\alpha\beta}$  falls inside the  $90^\circ \leq \theta_e \leq 270^\circ$  arc sector.

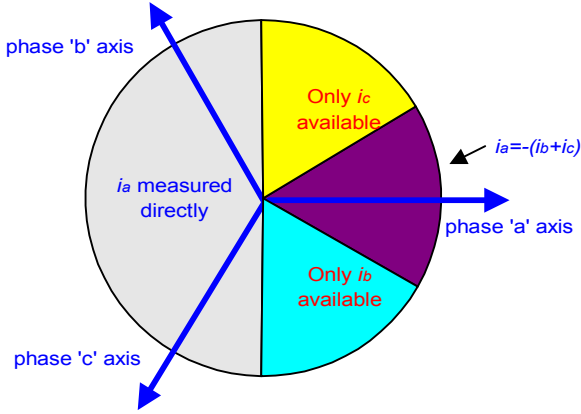


Fig. 7: Complex current vector plane illustrating arc sectors in which the phase *a* current  $i_a$  is measurable.

In addition,  $i_a$  can be indirectly measured using measurements of the other two phase currents  $i_{b\_FET}$  and  $i_{c\_FET}$  whenever the current vector falls inside the  $-30^\circ \leq \theta_e \leq +30^\circ$  arc sector by developing the inverted sum of those measurements.

Summarizing,  $i_a$  is measurable when the current vector falls within two arc sectors spanning a total of 240 deg-elec according to the following expressions:

$$i_{a\_m} = i_{a\_FET} \quad \text{for } 90^\circ \leq \theta_e \leq 270^\circ \quad (2)$$

$$i_{a\_m} = -(i_{b\_FET} + i_{c\_FET}) \quad \text{for } -30^\circ \leq \theta_e \leq +30^\circ \quad (3)$$

where the '*m*' subscript indicates the measured phase current, and the '*FET*' subscript indicates the current measured using the pilot current sensor in the lower half of the associated phase-leg.

However, the determination of  $i_a$  in the two remaining 60° intervals is more difficult because only one phase current flows through the low-side switches (either  $i_{b\_FET}$  or  $i_{c\_FET}$ ) during these two arc sectors.

Similar arguments apply to identify the regions of measurability for the other two phase currents. As a result, Fig. 8 provides a summary of the phase currents that can be

measured, directly or indirectly, in each of the six 60 deg-elec arc sectors. This figure clearly indicates that there are three sectors in which all three of the phase currents are measurable (directly or indirectly), but they are interspersed with three sectors in which only one phase current is measurable.

To overcome this limitation, two key assumptions are introduced. The first assumption is that the bandwidth of the current regulator is sufficiently high for the desired fundamental frequency that the angle of the actual complex current vector  $i_{\alpha\beta}$  exactly matches that of the current vector reference  $i_{\alpha\beta}^*$  at every time instant (i.e.  $\theta_e = \theta_e^*$ ). The second assumption is that the loading is perfectly symmetric, including the effect of disturbances.

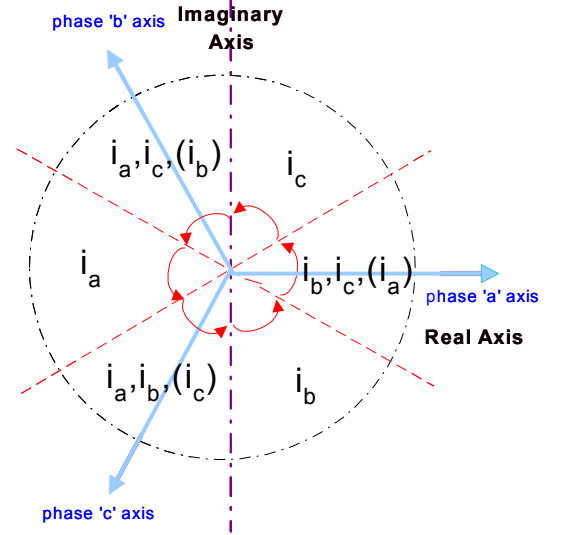


Fig. 8: Complex current vector plane illustrating measurable currents in each of the six 60 deg-elec arc sectors. Currents in parentheses are measured indirectly as an inverted sum of the other two.

Using these assumptions, one measured phase current is sufficient to calculate the amplitude of the two remaining phase currents that are not measured at that time instant. For example, consider the arc sector  $270^\circ \leq \theta_e^* \leq 330^\circ$  in which only  $i_b$  is measurable, but  $i_a$  is not. With perfect symmetry, the measured phase *b* current  $i_{b\_m}$  can be expressed as follows:

$$i_{b\_m} = |i_{\alpha\beta}| \cos(\theta_e - 120^\circ) \quad (4)$$

Applying the assumption described above that  $\theta_e = \theta_e^*$  yields

$$i_{b\_m} = |i_{\alpha\beta}| \cos(\theta_e^* - 120^\circ) \quad (5)$$

which can be solved to get

$$|i_{\alpha\beta}| = \frac{i_{b\_m}}{\cos(\theta_e^* - 120^\circ)} \quad (6)$$

The reconstructed value of the phase  $a$  current  $i_{a\_r}$  can be developed using the following defining expression

$$i_{a\_r} = |i_{\alpha\beta}| \cos(\theta_e) = |i_{\alpha\beta}| \cos(\theta_e^*) \quad (7)$$

where both assumptions are again applied.

Combining (6) and (7) then yields the final expression for the reconstructed value of  $i_a$  within the  $270^\circ \leq \theta_e^* \leq 330^\circ$  arc sector:

$$i_{a\_r} = i_{b\_m} \frac{\cos(\theta_e^*)}{\cos(\theta_e^* - 120^\circ)} \quad \text{for } 270^\circ \leq \theta_e^* \leq 330^\circ \quad (8)$$

Using the same approach, the unmeasurable phase  $a$  current can be reconstructed during the  $30^\circ \leq \theta_e^* \leq 90^\circ$  arc sector when only the phase  $c$  current is measurable ( $i_{c\_m}$ ) as follows:

$$i_{a\_r} = i_{c\_m} \frac{\cos(\theta_e^*)}{\cos(\theta_e^* + 120^\circ)} \quad \text{for } 30^\circ \leq \theta_e^* \leq 90^\circ \quad (9)$$

For the other two arc sectors, the reconstruction algorithm uses the available direct and indirect measurements of the phase  $a$  current provided by the pilot current sensors, according to the expressions provided earlier in (2) and (3)

$$i_{a\_r} = i_{a\_m} = i_{a\_FET} \quad \text{for } 90^\circ \leq \theta_e \leq 270^\circ \quad (10)$$

$$i_{a\_r} = i_{a\_m} = -(i_{b\_FET} + i_{c\_FET}) \quad \text{for } -30^\circ \leq \theta_e \leq +30^\circ \quad (11)$$

Reconstruction of the other two phase currents follows exactly the same procedure. Expressions in the form of (8) or (9) are used to estimate the two unmeasured currents in each of arc sectors where only one of the phase currents is measurable, while expressions in the form of (10) and (11) provide measurements of the phase currents in the other two arc sectors. Using this approach, the reconstruction algorithm is capable of delivering continuous feedback signals for each of the three phase currents over the entire  $360^\circ$  interval.

## V. EXPERIMENTAL TEST EQUIPMENT

Fig. 9 shows a block diagram of the current-regulated control scheme implemented in the experimental test equipment using a three-phase  $R$ - $L$  load. The control scheme uses the well-known synchronous-frame complex vector current regulator configuration, including provisions to decouple the synchronous frequency-dependent cross-coupling and the resistive voltage terms [9].

The three-phase PWM inverter uses three integrated pilot current sensors in the lower phase-leg switches as shown earlier in Fig. 1. The same 400V, 10A power MOSFETs discussed in Section II (Model IRFC740) are used for the lower inverter switches. The PWM frequency is 16 kHz and the regulator gain parameters are set to achieve a current regulator bandwidth of approximately 2 kHz.

Current feedback signals from the three pilot current sensors  $i_{abc\_FET}$  are fed to a special algorithm (highlighted by a heavy dotted line in Fig. 9) that performs the necessary operations to assemble the complete phase current waveforms. More specifically, the algorithm reconstructs the phase current waveforms using the technique described in Section IV whenever the corresponding phase currents cannot be directly or indirectly measured.

Information on the instantaneous phase angle command  $\theta_e^*$  is also provided to this algorithm in order for it to perform its reconstruction tasks. On the other hand, this algorithm simply passes the feedback signals from the pilot current sensors on to the regulator whenever valid phase current measurements are available from the pilot sensors.

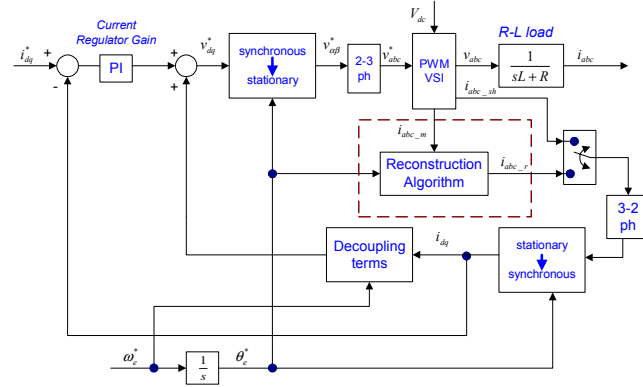


Fig. 9: Block diagram of synchronous-frame current regulator using reconstructed pilot current feedback

For these tests, the  $q$ -axis reference current  $i_q^*$  was held at zero so that  $i_d^*$  alone determines the amplitude of the phase currents. A passive, three-phase wye-connected  $R$ - $L$  load ( $R = 20 \Omega$ ,  $L = 4.2$  mH per phase) with a floating neutral was connected at the output terminals of the inverter. The inverter dc link input voltage was set at 130 Vdc.

A complete set of phase current measurements is generated independently in the test circuit for comparison with the reconstructed current. For this purpose, three small shunt resistances are inserted in series with the three low-side inverter switches and the resulting shunt voltages are measured. Since each shunt resistor captures the current flowing through both the low-side MOSFET switch and its anti-parallel diode, both polarities of phase current are measured. As a result, a complete set of phase current measurements can be assembled by sampling the voltage drop across the three shunt resistances during each zero (000) voltage vector. This measured shunt current vector is called  $i_{abc\_sh}$  in the Fig. 9 block diagram.

A selector switch that appears in Fig. 9 makes it possible to choose either the reconstructed pilot currents  $i_{abc\_r}$  or the measured shunt currents  $i_{abc\_sh}$  for the regulator feedback current and for the decoupling signals.

## VI. EXPERIMENTAL RESULTS

Using this equipment, the reconstructed pilot phase current for phase  $a$  is compared with the shunt-measured phase  $a$  current both for steady-state and transient step operation as shown in Figures 10 and 11. The traces in Fig. 10 show experimental results using the shunt-measured phase currents  $i_{abc\_sh}$  as feedback to the current regulator. The traces in Fig. 11 show the experimental results for the same test conditions except that the reconstructed currents  $i_{abc\_r}$  derived from the pilot current sensors are used as feedback to the current regulator.

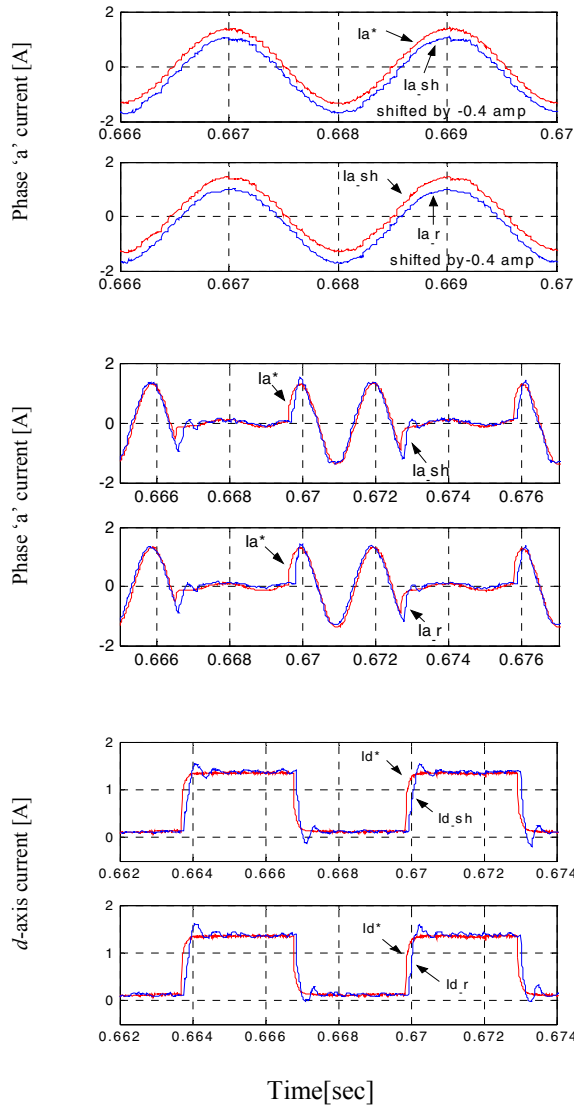


Fig. 10: Comparison of measured shunt and reconstructed pilot sensor currents in steady state (top) and with 1 A step commands in stationary frame (center) and synchronous frame (bottom). Conditions: 500 Hz fundamental frequency, current regulator BW: 2kHz,  $f_{sam}$ :16kHz with measured shunt current as feedback.

The topmost set of trace comparisons in both figures show the test results for phase  $a$  current during steady-state

operation at a fundamental frequency of approximately 500 Hz. A small offset is artificially introduced for one of the waveforms in each pair to make it easier to distinguish the features of each waveform.

The middle set of traces in Figs. 10 and 11 show the dynamic test results for the same phase when a step changes of approximately 1 Amp is applied in the  $d$ -axis current while keeping the  $q$ -axis current reference at zero. The bottom set of traces show the transformed  $d$ -axis current in the synchronous reference frame representing the combined effect of all three phase current measurements from the shunt and pilot sensors for the same step commands as in the previous case. For these

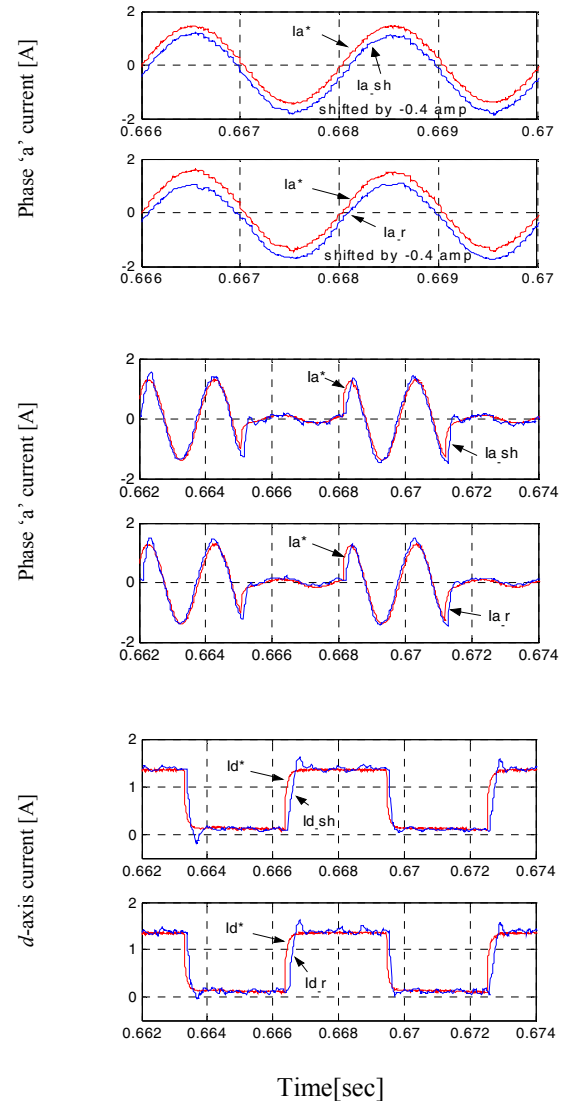


Fig. 11: Comparison of measured shunt and reconstructed pilot sensor currents in steady state (top) and with 1 A step commands in stationary frame (center) and synchronous frame (bottom). Conditions: Same test conditions as in Fig. 10, except with reconstructed pilot sensor current as feedback.

dynamic test results, the shunt and pilot sensor currents are compared individually with the commanded reference current

waveform in the stationary (middle traces) and synchronous (bottom traces) reference frames.

Examination of the waveform comparisons in Figs. 10 and 11 indicate that the reconstructed current waveforms using the pilot sensor measurements exhibit very closely matches the measured shunt current waveforms for both the steady-state and dynamic test conditions. Significantly, these tests show that the current regulator continues to perform very well when the reconstructed pilot phase currents are used for feedback (Fig. 11) instead of the measured shunt values (Fig. 10).

Experimental results in Fig. 12 and Fig. 13 show the sensitivity of the algorithm to load parameter variation. The

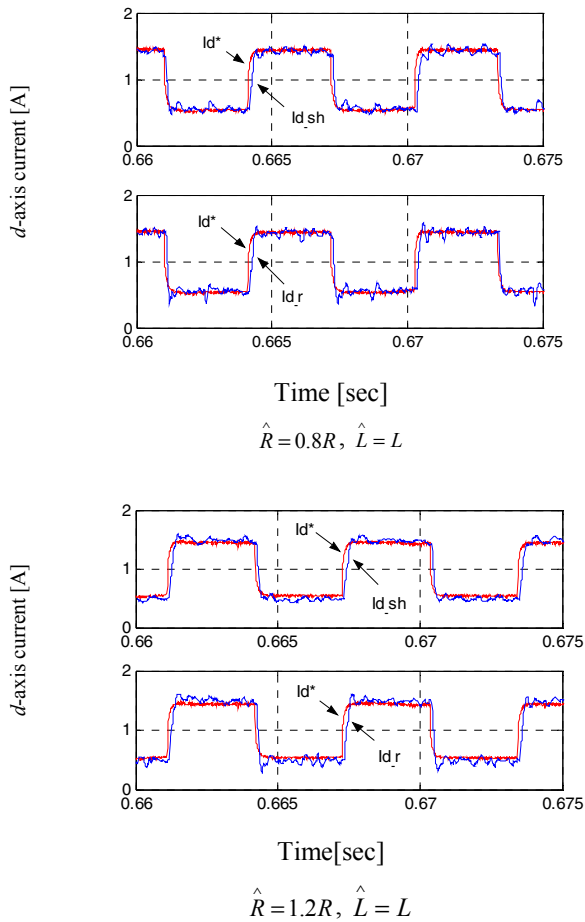


Fig. 12: Effects of error in estimated load resistance on measured shunt and reconstructed pilot current waveforms for 1 A step change in reference current. Same test conditions as in Fig.10, with reconstructed pilot current as feedback.

estimated resistance and inductance values are used in the current regulator to decouple the voltage drops associated with the load resistance and the frequency-dependent cross-coupling terms as indicated in Fig. 9. In the presence of inaccurate load parameter estimates, the current regulator does its best to correct for the resulting error voltages caused by the parameter inaccuracy.

Test results shown in both the figures are generated with the reconstructed pilot sensor currents used as feedback to the current regulator for a *d*-axis current reference step change of approximately of 1 Amp. Figure 12 shows the *d*-axis reconstructed pilot current and the *d*-axis measured shunt current in the synchronous frame compared with the reference current for a 20% error ( $\pm$ ) in the estimated resistance value while the inductance parameter is known correctly. Fig. 10 produces the same set of comparisons for the complementary conditions with  $\pm 20\%$  errors in the estimated inductance.

The waveforms in Figs. 12 and 13 indicate that the reconstructed pilot current matches the measured shunt current very well for the four tested cases of parameter estimation

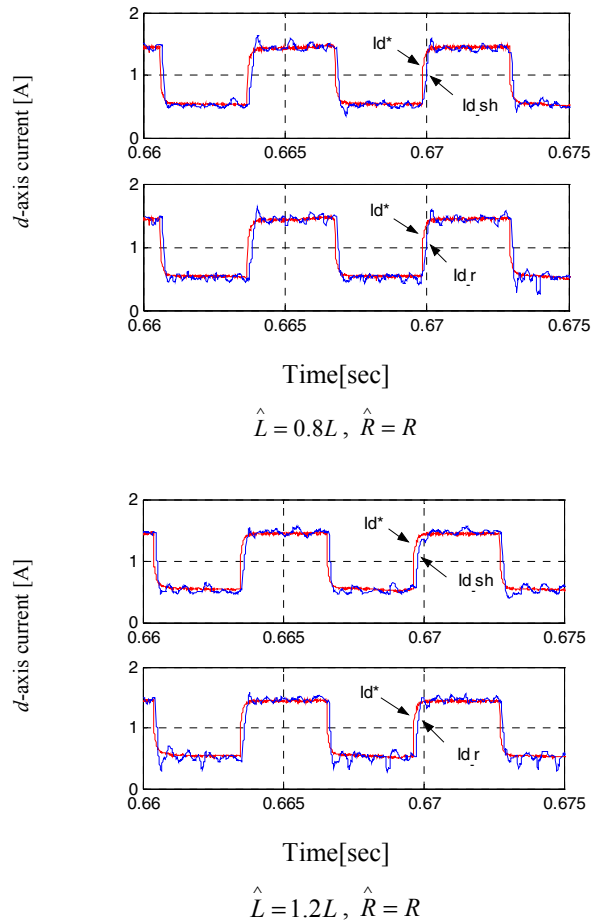


Fig. 13: Effects of error in estimated load inductance on measured shunt and reconstructed pilot current waveforms for 1 A step change in reference current. Same test conditions as in Fig.10, with reconstructed pilot current as feedback.

errors. In addition, it can be observed that these waveforms exhibit low sensitivity to the load parameter estimation errors. This is achievable because the current regulator has sufficiently high bandwidth to compensate for the parameter estimation inaccuracy.

## VI. CONCLUSIONS

A new current reconstruction algorithm for three-phase inverters using integrated pilot current sensors in the three low-side switches has been presented in this paper. As described in the preceding sections, there are three 60 deg-elec intervals each cycle when the reconstruction algorithm must derive two of the three phase current since the pilot current feedback is incomplete. Experimental results presented in Section V demonstrate that the proposed reconstruction algorithm is capable of providing the necessary current feedback signals to achieve high-performance current regulator performance with symmetric  $R$ - $L$  loads, despite the incomplete sensor measurements.

Further work is now under way to apply the pilot sensor configuration and the reconstruction techniques to ac machine drive applications and to consider the effect of disturbances. The back-emf waveforms of the machine loads differentiate them in a significant way from the passive  $R$ - $L$  loads considered in this paper. These back-emf voltages can be considered as major disturbance sources embedded in the loads, making it necessary to modify the reconstruction algorithm reported here. Progress with this extended work will be reported in a future paper.

The ultimate objective of this project is to develop the underlying technology such that pilot current sensors can be integrated into the low-side switches and become a viable replacement for the classical, bulky isolated Hall effect current sensors that are presently the de facto standard in high-performance inverter applications. Accordingly, this work represents progress towards providing an appealing means for incorporating low-cost current sensors directly into future power module designs, setting the stage for integrating complete current regulation capabilities inside each module.

## ACKNOWLEDGEMENT

The authors thank the Wisconsin Electric Machines and Power Electronics Consortium (WEMPEC) for use of its laboratory facilities in carrying out this investigation.

## REFERENCES

- [1] E.R. Olson and R.D. Lorenz, "Integrating Giant Magnetostrictive Current and Thermal Sensors in Power Electronic Modules," *Proc. of IEEE APEC Conference*, Miami Beach, Feb. 9-13, 2003, pp. 773-777.
- [2] F. Blaabjerg, J.K. Pedersen, U. Jaeger, P. Thøgersen, "Single current sensor technique in the DC-link of three-phase PWM-VS inverters. A review and the ultimate solution", *Proc. of IEEE Industry Applications Society Annual Meeting*, Oct. 1996, pp. 512-522.
- [3] F. Parasiliti, R. Petrella, M. Tursini, "Low cost phase current sensing in DSP based AC drives," *Proc. of IEEE International Symposium on Industrial Electronics (ISIE)*, Vol. 3, 1999, pp. 1284-1289.
- [4] T. G. Habetler, D. M. Divan, "Control strategies for direct torque control using discrete pulse modulation", *Proc. of IEEE Industry Applications Society Annual Meeting*, 1989, Page(s): 512-522.
- [5] T.M. Jahns and E.J. Wildi, "Integrated Current Sensor Configurations for AC Motor Drives," U.S Patent 4777579, Oct. 11, 1988.
- [6] T.P. Chow, D. N. Pattanayak, E.J. Wildi, J.M Pimbley, B.J Baliga, and M.S Adler "Design of current sensors in IGBT's," paper VIA-6, *Proc. of Device Research Conference*, Boston, MA, June, 1992.
- [7] *A IRC740 with Standard Packaging*, Datasheet from International Rectifier Corp., El Segundo, CA.
- [8] V. Blasko, V. Kaura and W. Niewiadomski, "Sampling methods for discontinuous voltage and current signals and their influence on bandwidth of control loops of electrical drives", *Proc. of IEEE Applied Power Electronics Conference (APEC)*, Feb. 1997, pp. 520-526.
- [9] F. Briz, M.W. Degner, and R.D. Lorenz, "Analysis and Design of Current Regulators Using Complex Vectors", *IEEE Trans. on Ind. Appl.*, Vol. 36, No. 3, May/June 2000 pp 817-825.